Proceedings 10th NUMGE 2023
10th European Conference on Numerical Methods in Geotechnical Engineering
Zdravković L, Konte S, Taborda DMG, Tsiampousi A (eds)
ISSN
© Authors: All rights reserved, 2023
https://doi.org/10.53243/NUMGE2023-109

Finite element formulations for implicit beam-to-solid coupling: numerical obstacles and solution strategies

A.-N. Granitzer[1] and F. Tschuchnigg[1]

[1]*Institute for Soil Mechanics, Foundation Engineering, and Computational Geotechnics, Graz University of Technology, Graz, Austria*

ABSTRACT: Due to their exceptional ability to simplify the finite element analysis of complex geotechnical problems involving a high number of slender structures, embedded beam formulations representing implicit beam-to-solid finite elements have attracted widespread interest from the scientific community. While numerous scientific contributions confirm their suitability for the modelling of pile-type structures in the light of load-settlement analyses, insight to the numerical phenomenon of oscillations traditionally occurring in the predicted skin traction profiles is rare. This numerical obstacle is the core of the present work, in which we perform parametric studies to investigate selected features of the recently developed embedded beam element with interaction surface, an improved version of the well-known embedded beam element with interaction line employed in the FE code Plaxis 3D. The results provide numerical evidence on the cause of the oscillatory nature, and shed light on potential solution strategies; moreover, they provide guidance with respect to future lines of research to achieve more genuine solutions.

Keywords: beam-to-solid coupling; embedded beam formulations; pile; numerical oscillations

1 INTRODUCTION

The numerical simulation of compound structures, i.e. structures involving a high number of rather one-dimensional slender structures, tied to spatial solid continua is a non-trivial task during the development and design phase of many geotechnical problems; piled rafts and soil nailing walls are a case in point, in which simulation engineers seek to strike a balance between acceptable computational expense and adequate calculation fidelity. In view of the finite element modelling approach, embedded beam formulations (EBF) have become the main workhorse for predicting the response of geotechnical compound structures; in this respect, numerous examples demonstrate the robustness and accuracy of EBF (e.g. Tschuchnigg, 2013), as well as their applicabilty to complex boundary value problems (BVP); for example, see Granitzer et al. (2021, 2022) and Scarfone et al. (2020).

In comparison to the modelling techniques available for embedding slender structures into a background solid mesh representing the soil domain, EBF combine several desireable features of practical relevance, such as a significant reduction of unknowns in the final system of equations resulting in a considerable reduction of computational burden, a high level of flexibility in the mesh generation procedure or the simplified evaluation of stress resultants based on well-established beam theories.

From a numerical point of view, EBF-type finite elements (FE) represent a special group of overlapping domain decomposition methods (ODDM) (Cai, 2003) which provide the general framework for coupling 1D beam FE with 3D solid FE by means of well-posed coupling schemes. Since ODDM employ some simplified model assumptions regarding the boundary conditions at the coupling zone between the two interacting FE types, however, applying EBF in finite element analyses (FEA) may trigger numerical inconsistencies that have adverse consequences in the interpretation of results (Granitzer and Tschuchnigg, 2021). To this date, EBF have been mainly validated and improved with the aim to capture the global response of benchmark solutions (e.g. Engin et al., 2007), whereas the non-physical evolution of numerical oscillations (NO) in the predicted skin traction profiles (STP) has received only little attention in the literature.

In this work, we investigate links between selected implementational features of EBF and arising NO on the basis of parametric studies, combined with a cycle-by-cycle measure to quantify the oscillatory amplitudes in the computed STP. The results pinpoint the efficacy of selected measures to reduce NO to an acceptable limit, and provide insight to their numerical origin.

2 BACKGROUND

Before we study numerical oscillations induced by EBF, clarity must exist about the principal components and coupling formalism of the EBF under consideration; moreover, we give a concise overview with respect to the current state of knowledge regarding NO evolving at the interface between adjoining subdomains.

In the current work, we distinguish between two EBF types, namely the embedded beam FE with interaction line (EB) after Tschuchnigg and Schweiger (2015), and the embedded beam FE with interaction surface (EB-I), which has been first introduced by Turello et al. (2016), and subsequently extended by Smulders et al. (2019). Unless otherwise stated, emphasis is placed on the latter, which can be regarded as generalized form of the EB; denoting R as the beam radius and $\Omega_{(\cdot)}$ as $(\cdot)$-EBF type, this can be exemplified by $\lim_{R\to 0} \Omega_{EB-I} = \Omega_{EB}$.

2.1 Problem formulation and coupling formalism

From a geometrical point of view, both EBF considered in this work consist of 1D beam FE which are coupled to an interaction zone Γ_c embedded in a 3D domain composed of solid FE. Adopting the principle of virtual work, contributions to the total virtual work of the mixed-dimensional system can be split into beam, solid and coupling terms. As a characteristic feature inherent to ODDM, the global solution to the BVP is approximated by iteratively solving the partial differential equations within the beam (Ω_b) and solid (Ω_s) subdomain, respectively, whereas the contributions to the total virtual work are independent of the coupling constraints (Steinbrecher et al., 2020); hence, well-established formulations for describing the interacting Ω_b and Ω_s can be used without modifications, together with powerful discretization techniques. In the present case, Ω_b is idealised as 3-noded Timoshenko beam FE, where each cross-section along the beam centerline is described by six degrees of freedom (DOF), three rotational and three translational ones, covering axial tension, bending, shear and torsion deformation modes (Meier et al., 2019). On the solid side, Ω_s is modelled as classical discretized 3D Boltzmann continuum, i.e. the nodes are equipped with three translational DOF.

Likewise, both EBF incorporate an intuitive L^2-coupling approach where the coupling constraints are formulated in terms of the beam $\tilde{\boldsymbol{u}}_b$ and solid $\tilde{\boldsymbol{u}}_s$ displacement fields evaluated at the coupling points $\tilde{\boldsymbol{x}}_i$ that are located on Γ_c. Under the hypothesis of perfect adherence, the coupling constraints read (Equation 1):

$$\tilde{\boldsymbol{u}}_b - \tilde{\boldsymbol{u}}_s = \boldsymbol{0}, \forall\, \tilde{\boldsymbol{x}}_i \in \Gamma_c \qquad (1)$$

which are enforced in the reference configuration using the penalty method (Wriggers, 2002), without the need to keep track of a surface normal vector in the current configuration; under axial loading, as considered in the following, the embedded interface stiffness in beam axis direction K_s is utilized to penalize the violation of coupling constraints. The existence of non-linear material models for describing Ω_s is naturally accounted for by model features which allow for the incorporation of a Coulomb-type failure criterion; moreover, K_s can be optionally defined in a stress-dependent manner considering a dimensionless scaling factor $\Gamma_s \in [0,1]$; cf. Tschuchnigg and Schweiger (2015). In this so-called layer-dependent configuration, the coupling terms are described by non-linear relations between energy-conjugate pairs of traction ($\tilde{\boldsymbol{t}}$) and relative displacement ($\boldsymbol{u}_{rel}$) variables, allowing for the analysis of STP.

The salient difference between the EB and EB-I model concerns the dimensionality of the beam-solid coupling zone, which can be classified as line-to-volume (1D-3D) and surface-to-volume (2D-3D) coupling problem, respectively. With regard to EB, $\tilde{\boldsymbol{x}}_i$ are placed along an interaction line $\Gamma_{c,1D}$, which coincides with the beam axis. On the contrary, EB-I formulate the coupling constraints at $\tilde{\boldsymbol{x}}_i$ that are distributed across an interaction surface $\Gamma_{c,2D}$, i.e. identical with the physical beam-solid contact surfaces; see Figure 1. Therefore, a consistent mapping scheme is introduced (Smulders et al., 2019), built on the assumption that the beam cross sections stay plane and unwarped throughout a simulation.

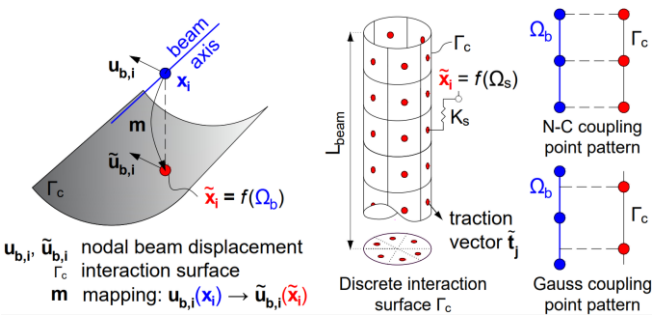

Figure 1. Mapping procedure of coupling constraint variable, interaction zone and coupling point pattern (EB-I)

Switching from 1D-3D to 2D-3D coupling has some beneficial consequences of practical relevance. For example, nodal moment loads in Ω_b no longer remain as beam nodal loads, but contribute to the solid load vector. In this way, EB-I allow for lifting the torsion-free assumption inherent to EB; Figure 2 supplements this application limit by additional loading situations where EB produce non-phyiscal results; for a more detailed discussion, the interested reader may refer to Hartl (2002) and Granitzer and Tschuchnigg (2022).

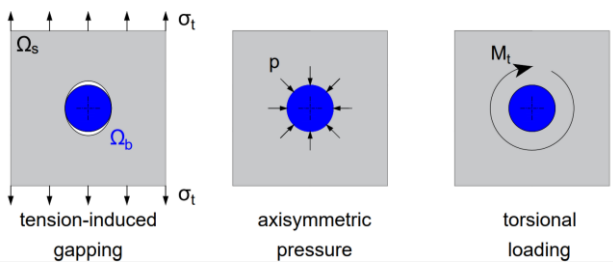

Figure 2. Loading situations where EB with 1D-3D coupling scheme produce non-physical results in the near-field of Ω_b

For brevity, the work carried out focuses on quasi-static problems. As a side note, however, it should be noted that both EBF are directly applicable to dynamic problems as well (Granitzer and Tschuchnigg, 2023).

2.2 Numerical skin traction oscillations

Artificially triggered numerical oscillations in the STP obtained at the interface between interacting solid FE have been revisited by many researchers, mainly in the light of continuous interface (CI) FE in which relative displacements between corresponding nodes constitute the primary coupling variables; cf. Schellekens and Borst (1993). In this context, the appropriate selection of integration schemes and interface stiffnesses has been found crucial to achieve genuine solutions to skin traction problems that involve plastic deformation.

Since EBF are equipped with point interfaces (PI) that conceptually differ from CI, beneficial observations made in the context of CI are not necessarily valid for PI. A striking difference stems from the fact that in PI considered in this work the $\tilde{\boldsymbol{t}}-\boldsymbol{u}_{rel}$ relations are evaluated at $\tilde{\boldsymbol{x}}_i$ located inside Ω_s. In lieu of using translational DOF stored at discrete nodes, this requires the projection of nodal information onto $\tilde{\boldsymbol{x}}_i$ through interpolation (both EBF) and weighted point-wise mapping (EB-I; Figure 1) to determine both $\tilde{\boldsymbol{u}}_s$ and $\tilde{\boldsymbol{u}}_b$.

Specific to the EB-I, another relevant aspect concerns the determination of beam-solid coupling contributions: Instead of an element-wise evaluation by numerical integration performed over Γ_c, the coupling contributions are seperately obtained at each $\tilde{\boldsymbol{x}}_i \in \Gamma_{c,2D}$, and subsequently assembled to the global system of equations; depending on the mesh configuration, the beam FE can therefore be connected to multiple solid FE intersecting with $\Gamma_{c,2D}$. Moreover, the integration scheme adopted has no influence on the structure of the element stiffness matrix, but controls the coupling point pattern (Figure 1); cf. Gens et al. (1989). To the best of the authors‘ knowledge, this aspect, along with a quantitative measure to describe NO in computed EBF STP will be discussed for the first time.

3 METHODOLOGY

3.1 Numerical analysis model

In the course of this work, the reponse of EBF is studied employing the well-known Alzey Bridge static pile load test reported in Sommer and Hambach (1974); see Figure 3 (a). The FEA are carried out using a research calculation kernel of the FE code Plaxis 3D (Bentley Systems, 2022). The EBF analysis domain is discretized with 6,329 10-noded tetrahedral solid FE with quadratic element functions. In an additional simulation, the pile domain is modelled as standard FE approach (SFEA), composed of zero-thickness CI attached to linear elastic (LE) solid FE forming Ω_b, which serves as numerical benchmark model; cf. Tschuchnigg (2013). A visual representation of all mesh configurations, as well as the material parameters considered for the Hardening Soil Small (HSS) model (Benz, 2007; Benz et al., 2009) and the layer-dependent EBF configurations can be found in Granitzer and Tschuchnigg (2021).

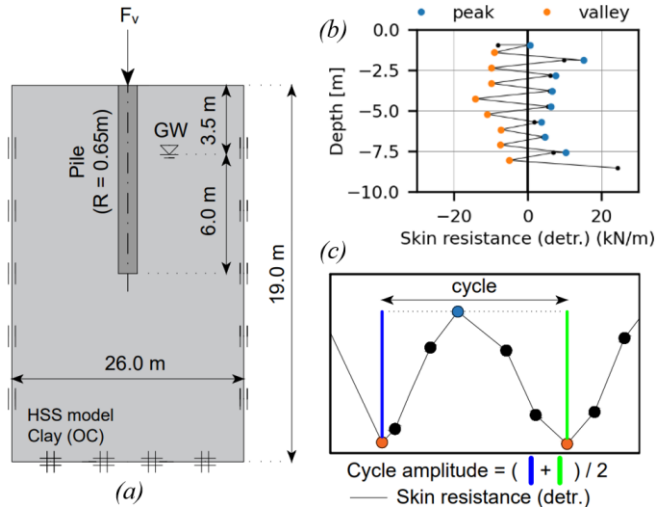

Figure 3. (a) FE model | cycle-by-cycle analysis procedure: (b) detrended STP and (c) cycle amplitude calculation.

3.2 Skin traction oscillation analysis

Traditionally, the assessment of NO related phenomena is restricted to the visual inspection of the skin and slip traction profiles. In an attempt to quantify the oscillatory features as function of selected numerical properties inherent to EBF, an intuitive cycle-by-cycle analysis algorithm is implemented in Python. The latter is inspired by the work of Cole and Voytek (2019), who have developed a similar approach to examine oscillations of neural signals in the time domain. Due to the different nature of the analysis domain, a key feature of the oscillation assessment method considered here is that it can be applied without the need to set a threshold for amplitude detection purposes, or a filter to remove noisy constituents in the raw data.

The first step in detecting NO is to detrend the stress-induced increase in skin traction from the raw data (i.e. sampled at the height of $\tilde{\boldsymbol{x}}_i$) to isolate the oscillatory components, such that they revert around a zero mean; see Figure 3 (b). Empirically, the moving average subtraction method with a window size of three (i.e. the number of nodes per beam FE) is found suitable for studying the problem. Subsequently, the detrended profiles are segmented into cycles identified by successive peaks, troughs, and zero-crossings. The cycles are chosen to start and end at penultimate beam FE with respect to both pile ends (i.e. excessive oscillations traditionally occuring at the sliding fronts, and caused by steep stress gradients, are not considered). As key outcome, the cycle amplitudes are computed as average detrended skin traction magnitude difference between extreme values of each cycle; cf. Figure 3 (c). The accumulated cycle amplitude distribution (CAD) allows for an intuitive analysis of EBF related parameters that are potentially relevant to NO, with the aim to explore remedies that enable smooth STP.

3.3 Parametric studies

To identify relevant parameters that amplify the formation of NO, and gain insight to the cause of this obstacle, sensitivity studies on selected parameters are performed. Key parameters that are tested include the EBF model type, mesh configuration, vertical loading magnitude, circumferential coupling point number (CIP; i.e. $\tilde{\boldsymbol{x}}_i$ placed along the cross-sectional beam circumference), integration scheme and skin traction failure criterion. Unless otherwise stated, all FEA are performed using a vertical loading magnitude of 1 MN.

4 RESULTS AND DISCUSSION

The phenomenon of numerical oscillations in STP of EBF is studied in Figures 4–9. All figures include the simulation results obtained with the EB-I (CIP=8, 3-point Newton-Cotes integration scheme; cf. Figure 1). In accordance with the observations made in previous studies, the SFEA provides STP that remain smooth along the whole pile length, except for peak oscillations occuring near the pile ends; this obstacle is attributed to relatively large skin traction gradients localized in these regions, and is observed despite the incorporation of potential slip planes to overcome the effect of singular plasticity points (van Langen, 1991).

Figure 4 compares the results derived from the EB-I and EB. Along the majority of the pile length, both EBF predict skin tractions that are slightly higher compared to the SFEA benchmark. An additional parametric study (not shown) has indicated that a better agreement can be achieved by improving the $\tilde{\boldsymbol{t}}$–$\boldsymbol{u}_{rel}$ relations at $\tilde{\boldsymbol{x}}_i$ distributed over the base; however, this aspect is beyond the scope of this work, and will be addressed in the future. The CAD clearly shows that the NO obtained with the EB-I are smaller in amplitude compared to the EB. An interesting detail can be observed at the base where the EB-I predicts a skin traction concentration that must be regarded unrealistic. A similar problem discovered in the realm of ealier EB versions has been resolved by modifying the ratio between the embedded interface stiffnesses considered along the pile shaft and at the base (Tschuchnigg, 2013); this strategy, combined with an improved stress mapping scheme required to obtain the actual normal stress at $\tilde{\boldsymbol{x}}_i$ considered in the Coulomb-type failure criterion are subject of current research to increase the numerical fidelity of the EB-I.

Figure 5 demonstrates the numerical robustness of EB-I in terms of the mesh size effect, a key advantage compared to the EB. The same holds true for the CIP number, which only has a minor influence on the CAD (Figure 6). However, since this parameter may have an impact on additional aspects, such as the convergence behaviour or the computational efficiency, additional studies are in demand to give general recommendations. Figure 7 showcases the general tendency of increasing NO with increasing load level, together with the desired increase of mobilized skin resistance over pile depth.

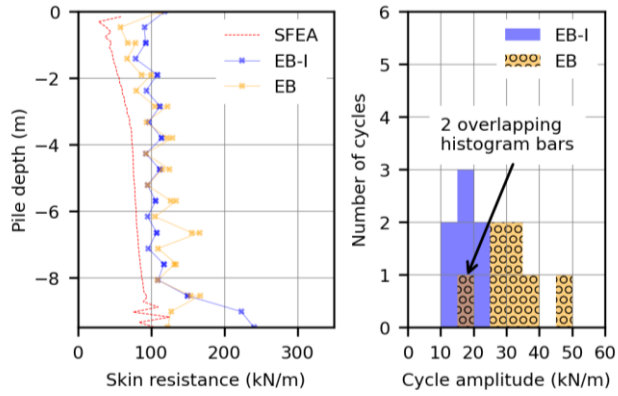

Figure 4. Skin traction profiles and cycle amplitude distribution obtained with SFEA, EB-I and EB

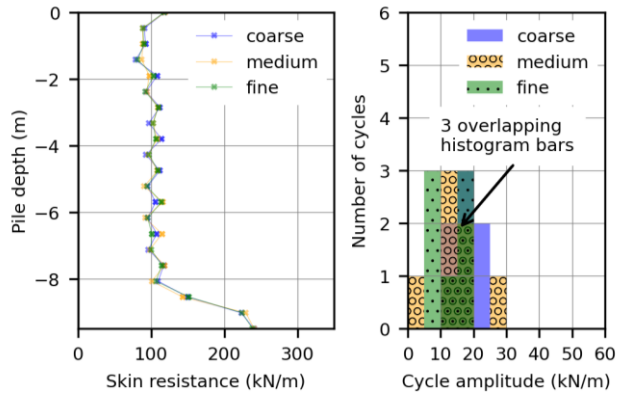

Figure 5. Skin traction profiles and cycle amplitude distribution obtained with varying mesh configurations (EB-I)

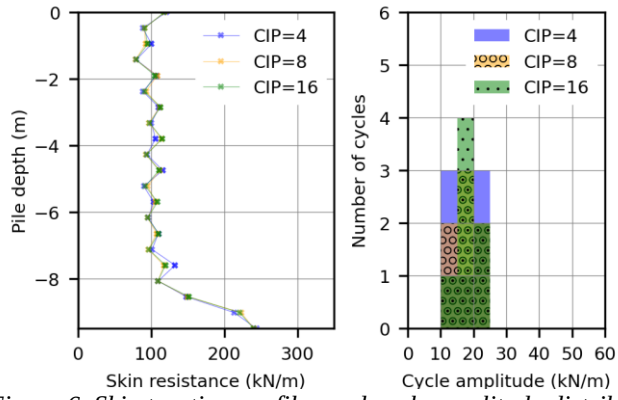

Figure 6. Skin traction profiles and cycle amplitude distribution obtained with varying coupling point number (EB-I)

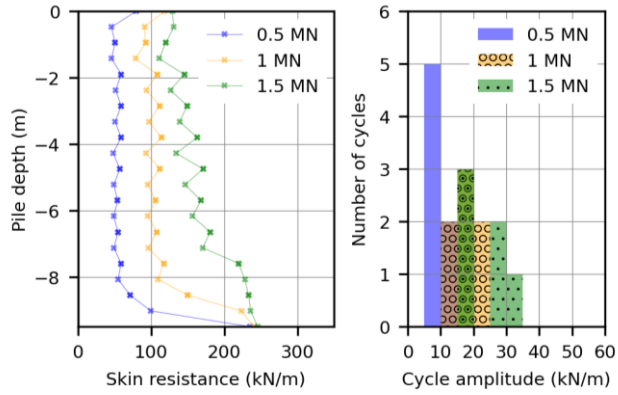

Figure 7. Skin traction profiles and cycle amplitude distribution obtained with varying vertical loading magnitude (EB-I)

The STP from Figure 8 are computed with the numerically integrated 2-point Gauss (Gauss) as well as the lumped 3-point Newton-Cotes (N-C) integration scheme; cf. Schellekens and Borst (1993). As illustrated in Figure 1, the integration scheme influences the geometrical CIP distribution, in particular at the lower pile end where Gauss-$\tilde{\boldsymbol{x}}_i$ no longer interesect with the pile base. It is clear from the results that the integration scheme has a significant effect on the CAD, whereas Gauss seems to be preferable from the practical point of view as it suppresses oscillatory components in the numerical predictions; it should be emphasized that this observation contradicts previous statements which have identified N-C as general remedy to avoid NO in STP of CI. This indicates that NO may be caused by numerical obstacles that are not relevant in CI.

In an additional study presented in Figure 9, the ultimate skin resistance is defined as unlimited (unlim), i.e. not coupled to the Coulomb-type limit (lim) criterion which causes the embedded interface stiffness at $\tilde{\boldsymbol{x}}_i$ to adopt zero values in the sliding case. While the CAD remains relatively unaffected, unlimiting the skin resistance in the current EB-I configuration has an adverse effect on the skin traction mobilized at the lowermost $\tilde{\boldsymbol{x}}_i$ (i.e. ignored in the CAD), where the spurious skin traction culmination is further amplified; this showcases the signficance of a reliable EBF failure criterion that will be subject of future research.

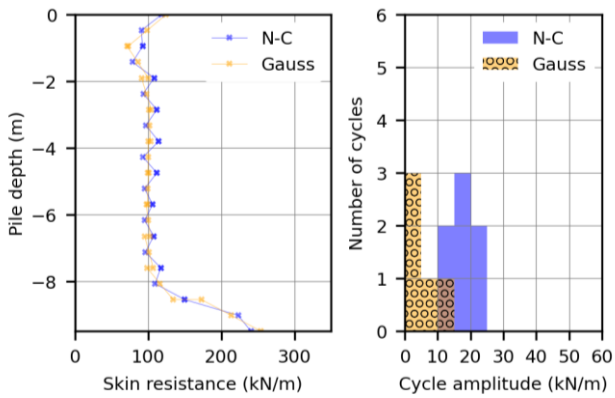

Figure 8. Skin traction profiles and cycle amplitude distribution obtained with varying integration scheme (EB-I)

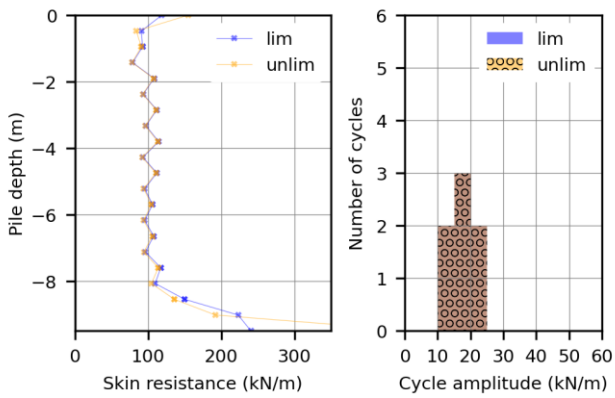

Figure 9. Skin traction profiles and cycle amplitude distribution obtained with varying failure criterion (EB-I)

Preliminary studies not presented here provide numerical evidence that NO also occur for LE soil conditions and constant embedded interface stiffnesses. This implies that NO are an intrinsic feature of the EBF considered, rather than a numerical obstacle triggered by a certain combination of modelling parameters. It can be further concluded that NO are attributed to the non-smoothness of the relative displacement fields, i.e. the relative deformation between Ω_b and Ω_s computed at $\tilde{\boldsymbol{x}}_i \in \Gamma_c$. As $\tilde{\boldsymbol{u}}_b$ is approximated on the basis of Hermite polynomials (i.e. approximated displacement fields are C^1-continous), NO are caused by the relatively poor intra-element interpolation of $\tilde{\boldsymbol{u}}_s$. This is exemplified by Figure 10 where selected solid FE element functions are evaluated along the beam axis ξ, employing a projection χ_h from a point on ξ onto the corresponding point in Ω_s. Obvisouly, they represent nonlinear functions, with strong and weak dicontinuities at ξ_s and ξ_w (i.e. jumps at points where Ω_b sticks out of Ω_s, and kinks at points where Ω_b crosses solid FE boundaries). Numerically integrated solid-beam coupling terms therefore contain integrands that are not of polynomial degree, giving rise to integration errors; cf. Steinbrecher et al. (2020).

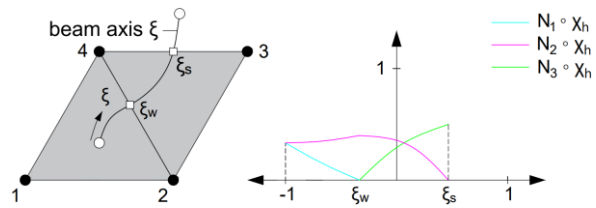

Figure 10. Patch of beam and solid elements: Projection of selected solid element function onto beam centerline.

The above discussion justifies two potential solution strategies to improve the EBF performance in terms of NO, both which are described in Goudarzi and Simone (2019). First, the application of advanced approximation techniques that allow for a more accurate estimation of $\tilde{\boldsymbol{u}}_s$, i.e. a computationally expensive process that impairs general deployment in engineering practice. The second strategy considered in Figure 11 concerns a reduction of the embedded interface stiffness magnitude.

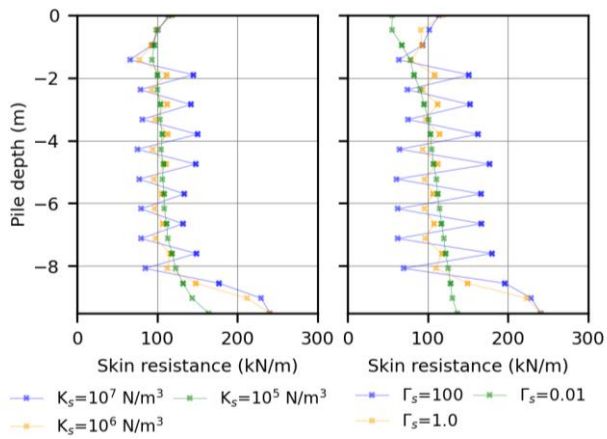

Figure 11. Skin traction profiles obtained with varying embedded interface stiffness magnitudes

5 CONCLUSION

Embedded beam formulations are prone to produce non-physical oscillations in the numerically predicted skin traction profiles. Parametric studies addressing this obstacle are at the core of this work, together with a discussion of the cause and potential solution strategies.

We conclude that oscillatory tendencies are attributed to limitations of the solid displacement field approximation. To some extent, this problem can be effectively circumvented by reducing the embedded interface stiffness magnitudes. However, this may have an influence on the global response as well, which should be addressed in future studies concerning the interface constitutive model. Future lines of research may also explore a more robust definition of the interface failure criterion.

6 ACKNOWLEDGEMENT

The work is part of an ongoing research cooperation between the Graz University of Technology and R&D unit of Seequent, the Bentley Subsurface Company.

7 REFERENCES

Bentley Systems. 2022. *Scientific Manual: Plaxis Connect Edition V22.02*.

Benz, T. 2007. *Small-Strain Stiffness of Soils and its Numerical Consequences*, PhD Thesis, Stuttgart.

Benz, T. Schwab, R. Vermeer, P. 2009. Small-strain stiffness in geotechnical analyses, *Bautechnik* **86(S1)**, 16–27, 10.1002/bate.200910038.

Cai, X. 2003. Overlapping Domain Decomposition Methods, *Advanced Topics in Computational Partial Differential Equations* (Eds: Barth, T.J., Griebel, M., Keyes, D.E. et al.), 57–95. Springer, Berlin.

Cole, S. Voytek, B. 2019. Cycle-by-cycle analysis of neural oscillations, *Journal of neurophysiology* **122(2)**, 849–861, 10.1152/jn.00273.2019.

Engin, H. Brinkgreve, R. Septanika, E. 2007. Improved embedded beam elements for the modelling of piles. *Numerical models in geomechanics: Proceedings, 10th International Symposium on Numerical Models in Geomechanics* (Ed: Pande, G.N.). Taylor & Francis, London.

Gens, A. Carol, I. Alonso, E.E. 1989. An interface element formulation for the analysis of soil-reinforcement interaction, *Computers and Geotechnics* **7(1-2)**, 133–151, 10.1016/0266-352X(89)90011-6.

Goudarzi, M. Simone, A. 2019. Discrete inclusion models for reinforced composites: Comparative performance analysis and modeling challenges, *Computer Methods in Applied Mechanics and Engineering* **355**, 535–557, 10.1016/j.cma.2019.06.026.

Granitzer, A.-N. Tschuchnigg, F. Summerer, W. Galler, R. Stoxreiter, T. 2021. Construction of a railway tunnel above the main drainage tunnel of Stuttgart using the cut-and-cover method, *Bauingenieur* **96(5)**, 156–164, 10.37544/0005-6650-2021-05-40.

Granitzer, A.-N. Rebhan, M.J. Tschuchnigg, F. 2022. Influence of Reaction System on Uplift Behaviour of Micropiles Subjected to Static Pullout. *Field Measurements in Geomechanics: Proceedings, 11th International Symposium on Field Monitoring in Geomechanics* (Ed: ISSMGE TC220). London.

Granitzer, A.-N. Tschuchnigg, F. 2021. Practice-Oriented Validation of Embedded Beam Formulations in Geotechnical Engineering. *Processes* **9(10)**, 1739, 10.3390/pr9101739.

Granitzer, A.-N. Tschuchnigg, F. 2022. On the Use of Embedded Beam Formulations for the Numerical Analysis of Deep Foundations. *Challenges and Innovations in Geomechanics: Proceedings, 16th IACMAG Conference - Volume 3* (Eds: Barla, M. Di Donna, A. & Sterpi, D.), 307–314. Springer, Cham.

Granitzer, A.-N. Tschuchnigg, F. 2023. Behaviour of Embedded Beam Formulations Under Dynamic Loading. *Proceedings, 5th ICNDSMGE* (Eds: Atalar, C. & Çinicioglu, F.), 353–361. Springer, Cham.

Hartl, H. 2002. *Development of a Continuum-Mechanics-Based Tool for 3D FEA of Reinforced Concrete Structures and Application to Problems of Soil-Structure Interaction*, PhD Thesis, Graz.

Meier, C. Popp, A. Wall, W.A. 2019. Geometrically Exact Finite Element Formulations for Slender Beams: Kirchhoff–Love Theory Versus Simo–Reissner Theory, *Archives of Computational Methods in Engineering* **26(1)**, 163–243, 10.1007/s11831-017-9232-5.

Scarfone, R. Morigi, M. Conti, R. 2020. Assessment of dynamic soil-structure interaction effects for tall buildings: A 3D numerical approach, *Soil Dynamics and Earthquake Engineering* **128**, 1–14, 10.1016/j.soildyn.2019.105864.

Schellekens, J. Borst, R. 1993. On the numerical integration of interface elements, *International Journal for Numerical Methods in Engineering* **36**, 43–66.

Smulders, C.M. Hosseini, S. Brinkgreve, R. 2019. Improved embedded beam with interaction surface. *Proceedings, 17th ECSMGE* (Eds: Sigursteinsson H., Erlingsson, S. & Bessason, B.), 1048–1055. COC, Reykjavík.

Sommer, H. Hambach, P. 1974. Großpfahlversuche im Ton für die Talbrücke Alzey, *Bauingenieur* **49**, 310–317.

Steinbrecher, I. Mayr, M. Grill, M.J. et al. 2020. A mortar-type finite element approach for embedding 1D beams into 3D solid volumes, *Computational Mechanics* **66(6)**, 1377–1398, 10.1007/s00466-020-01907-0.

Tschuchnigg, F. 2013. *3D Finite Element Modelling of Deep Foundations Employing an Embedded Pile Formulation*, PhD Thesis, Graz.

Tschuchnigg, F. Schweiger, H.F. 2015. The embedded pile concept – Verification of an efficient tool for modelling complex deep foundations, *Computers and Geotechnics* **63**, 244–254, 10.1016/j.compgeo.2014.09.008.

Turello, D.F. Pinto, F. Sánchez, P.J. 2016. Embedded beam element with interaction surface for lateral loading of piles, *International Journal for Numerical and Analytical Methods in Geomechanics* **40(4)**, 568–582, 10.1002/nag.2416.

van Langen, H. 1991. *Numerical analysis of soil-structure interaction*, PhD Thesis, Delft.

Wriggers, P. 2002. *Computational contact mechanics*. Wiley, Chichester.